Journal of Marine Research, 74, 249–276, 2016

Vorticity dynamics near sharp topographic features

by Bruno Deremble[1,2], William K. Dewar[1], and Eric P. Chassignet[1,3]

ABSTRACT

In ocean models, the interaction with boundaries is often parameterized as it involves small-scale processes that are usually hard to capture in a large-scale model. However, such interactions can play important roles in the model dynamics. For example, the choice of boundary conditions (free-slip vs. no-slip) has a direct impact on the vorticity (enstrophy) budget: with no-slip boundary conditions, vorticity is injected into the system, whereas with free-slip boundary conditions, there should be no vorticity injection as long as the coastline is smooth. However, we show here that at boundary singularities (e.g., corners), vorticity is injected into the domain even for free-slip boundary conditions. In this article, we use North Brazil Current rings to better understand the dynamics of eddy-topography interaction. This complex interaction is first analyzed in terms of a point vortex interacting with a wall. Within this simplified framework, we can describe the vorticity generation mechanism as a pseudoinviscid process. To quantify this vorticity injection, we first consider the inviscid limit for which we can derive an analytical formula. This theoretical prediction is then evaluated in conventional gridded ocean models. In such models, the representation of such a "viscous" boundary interaction may be affected by the grid representation and the discretization of the advection and viscous operators.

Keywords: vorticity conservation, point vortex, vortex sheet, singularities

1. Introduction

Eddies are ubiquitous in the ocean and play an important role in transporting heat and salt. They also contribute to closing the mechanical energy budget where energy is provided by the atmospheric forcing and dissipated via eddy viscosity. It has been argued (Dewar and Hogg 2010; Zhai, Johnson, and Marshall 2010) that a significant part of this energy loss takes place at the boundaries, but the interaction of eddies with topography is still a poorly understood process and is not well-represented in numerical models. There is a considerable difference in dynamics between the ocean interior and near the coastlines because of the lateral boundary conditions that are imposed at the topography. The drag exerted on the tangential flow greatly depends on how well the boundary layer is resolved, and the representation of the vorticity dynamics near topographic features in numerical models

1. Department of Earth, Ocean, and Atmospheric Science, Florida State University, Tallahassee, FL 32304.
2. Corresponding author: ***e-mail: bderemble@fsu.edu***
3. Center for Ocean-Atmospheric Prediction Studies, Florida State University, Tallahassee, FL 32306.

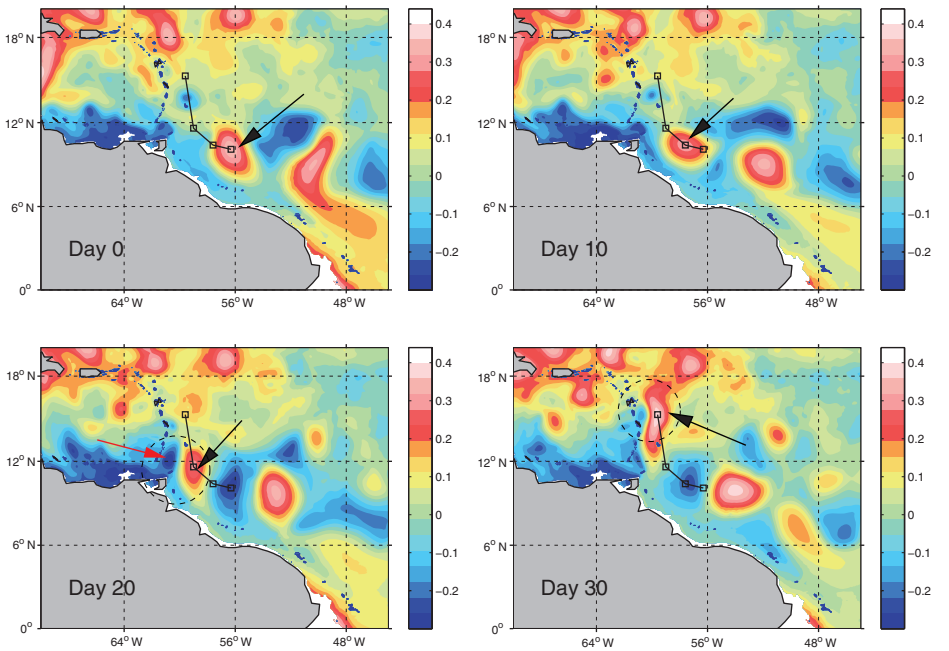

Figure 1. Sea surface height time evolution of a North Brazil Current (NBC) surface ring in the 1/25° global hybrid coordinate ocean model for a 30-day period in 2006. The NBC ring (indicated by a black arrow) centered in the upper left panel (day 0) takes approximately 20 days to reach the Lesser Antilles Island chain, traveling at a speed of $\sim$15 cm s^{-1}. Day 20 illustrates the formation of the cyclone (indicated by a red arrow) as the NBC ring leaves the continental shelf. The dipole, which consists of the cyclone coupled to the anticyclonic NBC ring, then moves rapidly northward by mutual advection (day 30). The squares connected by segments mark the position of the anticyclone on days 0, 10, 20, and 30. Color scale: centimeters.

will depend strongly on the choice of free- or no-slip boundary conditions. In this article, we consider the example of the North Brazil Current (NBC) rings to illustrate one aspect of eddy-topography interaction: vorticity dynamics near sharp topographic features. The northern coast of Brazil is a region of high eddy activity, in part because of the retroflection of the NBC. This retroflection is accompanied by the regular formation of rings that propagate northwestward along the coast of Brazil. The migration path of these rings is illustrated in Figure 1 where we plot four snapshots of the sea surface height (SSH) extracted from a high resolution (1/25°) global hybrid coordinate ocean model (HYCOM) simulation as a ring travels northward along the coast of Brazil.

The NBC ring centered in Figure 1(a) (day 0) takes approximately 20 days to reach the Lesser Antilles Island chain (Fig. 1b, day 10), traveling at a speed of $\sim$15 cm s^{-1} in agreement with observations (Fratantoni and Glickson 2002) and other numerical experiments (Garraffo et al. 2003). After day 20, the initial northwestward trajectory changes to a

northward trajectory (parallel to the chain of islands), and we notice an acceleration of the migration speed as the ring moves along the chain of islands (Fig. 1c). Among the factors that could play a role in this acceleration, we note the appearance of a cyclone in Figure 1(c) (red arrow) as the NBC ring leaves the continental shelf. The resulting dipole, consisting of the cyclone coupled to the anticyclonic NBC ring, then moves rapidly northward by mutual advection (Fig. 1d, day 30). The translation speed reached by the dipole (30 cm s^{-1}) is twice the speed of the anticyclone moving by itself along the South American coast (15 cm s^{-1}). This migration path has been confirmed with drifter observations (Fratantoni and Richardson 2006).

Close examination of satellite and model mean SSH variability shows two areas of high eddy activity that are separated by a gap of low variability: one along the South American coast and one further north along the island chain. We interpret the gap as further support for the sudden, rapid movement of NBC rings. We argue that the rapidly moving rings imprint less variability than slowly moving rings.

These observations motivate us to ask what mechanisms are responsible for the propagation and acceleration of NBC rings as they encounter the Caribbean Island arc. The apparent importance of the NBC rings in the net transport of the meridional overturning circulation (Johns, Zantopp, and Goni 2003) emphasizes the need to understand this aspect of their behavior; variations of this sort in propagation lead to heat and mass flux divergences that can be linked to climate variability. In the remainder of this article, we examine if the regional behavior of the rings is connected to the Brazilian coastal topography and the Caribbean Islands.

We now analyze the sequence of events depicted in Figure 1 in terms of a vorticity and potential vorticity (PV) formalism. In this framework, the anticyclonic ring corresponds to a patch of negative relative vorticity, whereas the newly created cyclone corresponds to a patch of positive vorticity. Hence, our goal is to understand the processes that led to the creation of this patch of positive vorticity. For an idealized two-dimensional (2d) flow, we can show that PV creation is a result of boundary interactions. In 2d, the incompressible Navier-Stokes equation in vorticity form is

$$\frac{\partial \omega}{\partial t} + \boldsymbol{u} \cdot \nabla \omega = \nu \nabla^2 \omega, \tag{1}$$

with $\omega = f + \nabla \times \boldsymbol{u}$ the vorticity (scalar in 2d), f the Coriolis parameter, and ν the kinematic viscosity. Note that there is no forcing term in this equation because we are interested in the free evolution of a prescribed initial vorticity field. From the Navier-Stokes equation in a bounded domain (with no-normal-flow boundary condition), we can derive equations for energy and enstrophy:

$$\frac{dE}{dt} = -2\nu Z, \tag{2}$$

with

$$E = \frac{1}{2}\int_S |\boldsymbol{u}|^2 ds, \tag{3}$$

the energy and with Z the enstrophy defined as

$$Z = \frac{1}{2}\int_S \omega^2 ds, \tag{4}$$

where the integral is computed over the entire domain.

The time evolution of enstrophy is given by

$$\frac{dZ}{dt} = -\nu \int_S |\nabla\omega|^2 ds + \nu \oint_{\partial S} \omega(\boldsymbol{n}\cdot\nabla\omega) dl. \tag{5}$$

The first term on the right-hand side is a sink of enstrophy proportional to the gradient of vorticity squared. The second term is exactly zero for free-slip boundary conditions, whereas for no-slip boundary conditions, it measures the rate of production of enstrophy by viscous effects at the boundary. In the limit of vanishing viscosity, both energy and enstrophy are then conserved.

This question of which boundary condition to choose (free-slip vs. no-slip) is a recurrent issue in the ocean modeling community (Verron and Blayo 1996; Adcroft and Marshall 1998). The most common way to implement the no-slip boundary condition is to set the tangential velocity at the boundary to zero. As a consequence, a boundary layer will develop to connect the interior flow with the boundary. If we consider an interior flow of magnitude U tangent to a wall, the thickness δ of the boundary layer will increase with the downstream (along wall) direction x as

$$\delta(x) = \sqrt{\frac{\nu x}{U}}, \tag{6}$$

which corresponds to the Blasius solution (see Kundu and Cohen 2008, chap. 10.5). In a turbulent ocean, the kinematic viscosity coefficient ν is usually chosen several orders of magnitude higher than the real kinematic viscosity for water: it is not rare to use a value of $\nu O(100\ \mathrm{m^2\ s^{-1}})$ as a parameterization of subgrid-scale phenomena (Reynolds stresses) in ocean models (e.g., Chassignet and Garraffo 2001; Chassignet and Marshall 2008). Thus, the thickness of the boundary will be of the order $\delta(x) = 10\sqrt{x}$ and may detach from the boundary to interact with interior flow. This difference between the free-slip limit and the no-slip boundary conditions has strong implications for the flow dynamics, especially for the vortex-topography interaction. Deremble et al. (2011) showed that if the grid size near the topography is greater than the width of the boundary layer, then the free-slip boundary condition is better suited to provide an accurate representation of the dynamics.

To illustrate the differences between the free-slip limit versus no-slip boundary conditions, we plot in Figure 2 the evolution of a vortex near a wall in a 2d model (see the full description

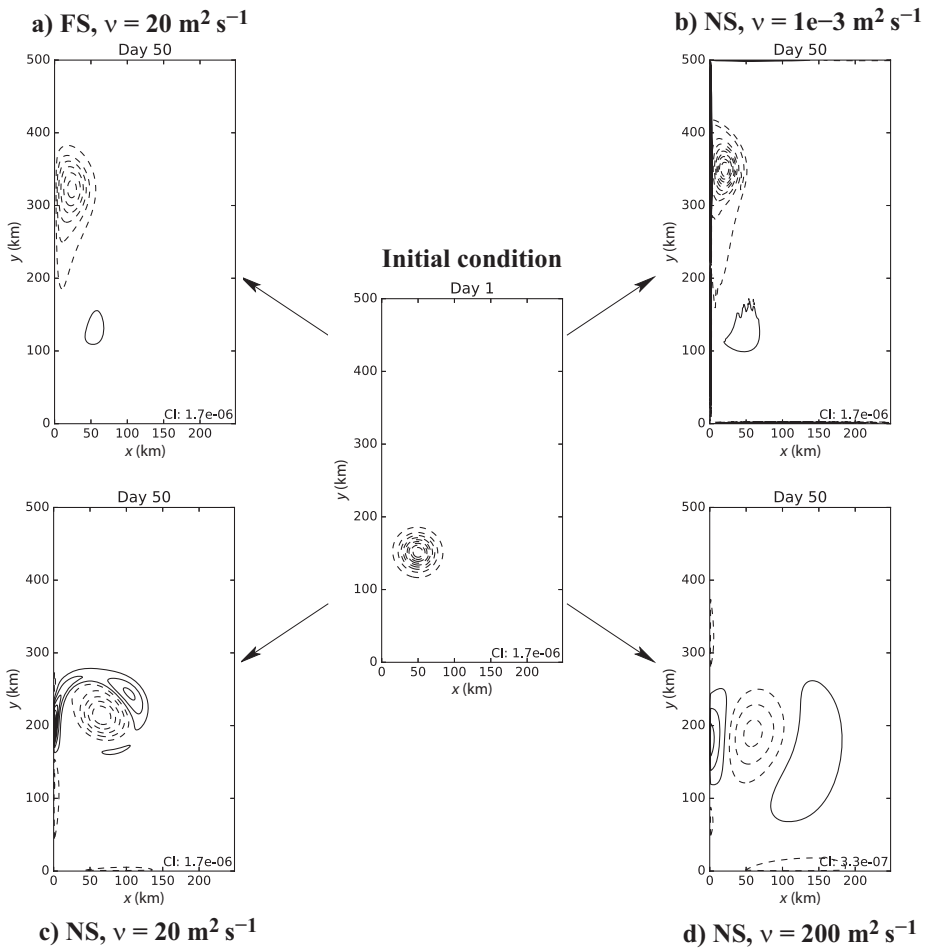

Figure 2. Different scenarios for the vortex-wall interaction: the center panel is the initial vorticity field. The other four panels are the final vorticity after 50 days with (a) free-slip (FS) boundary condition; (b) no-slip (NS), $\nu = 10^{-3}$ m^2 s^{-1}; (c) no-slip, $\nu = 20$ m^2 s^{-1}; and (d) no-slip, $\nu = 200$ m^2 s^{-1}. The contour interval is the same for all panels except for panel (d).

of the model in Section 2). The center panel shows the initial vorticity field. With free-slip boundary conditions (Fig. 2a), the vortex deforms because of the presence of the wall and propagates according to the image effect (Kundu and Cohen 2008). This scenario is independent of the value of the viscosity (not shown). With no-slip boundary conditions and weak viscosity ($\nu = 10^{-3}$ m^2 s^{-1}), the result is essentially the same except that there is an intense vortex sheet between the vortex and the wall (Fig. 2b). For a higher value of viscosity (Fig. 2c: $\nu = 20$ m^2 s^{-1}), the boundary layer is thicker (cf. equation 6) and detaches from the

wall. Finally, for even higher values of the viscosity (Fig. 2d: $\nu = 200\ \mathrm{m^2\ s^{-1}}$), the vortex stays in place and decays over time (note the different contour interval for this panel).

The question of vorticity generation at boundaries has been the focus of many studies (see, e.g., Morton 1984; Lundgren and Koumoutsakos 1999; Brøns et al. 2014) but has not received a lot of attention in the ocean community. In this article, we focus on the behavior of the flow near "singularities," by which we mean places where the curve describing the boundary is discontinuous in its derivative. We will investigate how such singularities lead to vorticity creation even in the inviscid free-slip limit.

2. Conceptual view of the NBC rings

The dynamics of NBC rings involve many complicated interactions (e.g., shape of the topography, stratification, forcing). In order to clarify the vorticity dynamics in this region, we simplify the situation depicted in Figure 1 as much as possible: we study the interaction of a barotropic (2d) vortex with a corner at a wall. The time integration of this model is shown in Figure 3 where the topography is represented with the gray area. The initial condition is a Gaussian patch of negative vorticity placed next to the wall (Lamb-Oseen vortex). In the relative frame of reference centered on the vortex, the flow field of this vortex in the absence of the wall is given by the azimuthal profile

$$v_\theta(r) = \frac{\Gamma}{2\pi r}\left[1 - \exp\left(-\frac{r^2}{2r_0^2}\right)\right], \tag{7}$$

with r_0 the pseudoradius of the vortex, and Γ the strength the vortex. The vorticity pattern corresponding to this velocity field is a Gaussian bump

$$\omega(r) = \frac{\Gamma}{2\pi r_0^2}\exp\left(-\frac{r^2}{2r_0^2}\right). \tag{8}$$

We use the MIT general circulation model (Marshall et al. 1997) to model the evolution of the vortex forward in time. The size of the domain is 500×500 km with a grid resolution of 1,250 m. We use a harmonic viscosity coefficient of $\nu = 20\ \mathrm{m^2\ s^{-1}}$ with free-slip boundary conditions and a time step of $\Delta t = 200$ s. The vortex corresponds to an anticyclone ($\Gamma = -5 \times 10^4\ \mathrm{m^2\ s^{-1}}$) of initial pseudoradius $r_0 = 20$ km. The initial vortex is placed next to the wall, which imposes a no-normal-flow boundary condition (Fig. 3a). The effect of this boundary condition is to deform the anticyclone such that the latter will propagate northward along the wall via the image effect (Kundu and Cohen 2008). At day 10 (Fig. 3b), the vortex reaches the corner, and we observe the creation of positive vorticity at the tip of the corner, which takes the form of a thin vortex filament that rolls up onto itself (day 20, Fig. 3c). Viscosity eventually smooths the filament into a uniform vortex patch with positive vorticity. This newly created patch forms a dipole with its anticyclonic partner, and the dipole moves according to its own dynamics (Fig. 3d). In fact, such dipoles are known

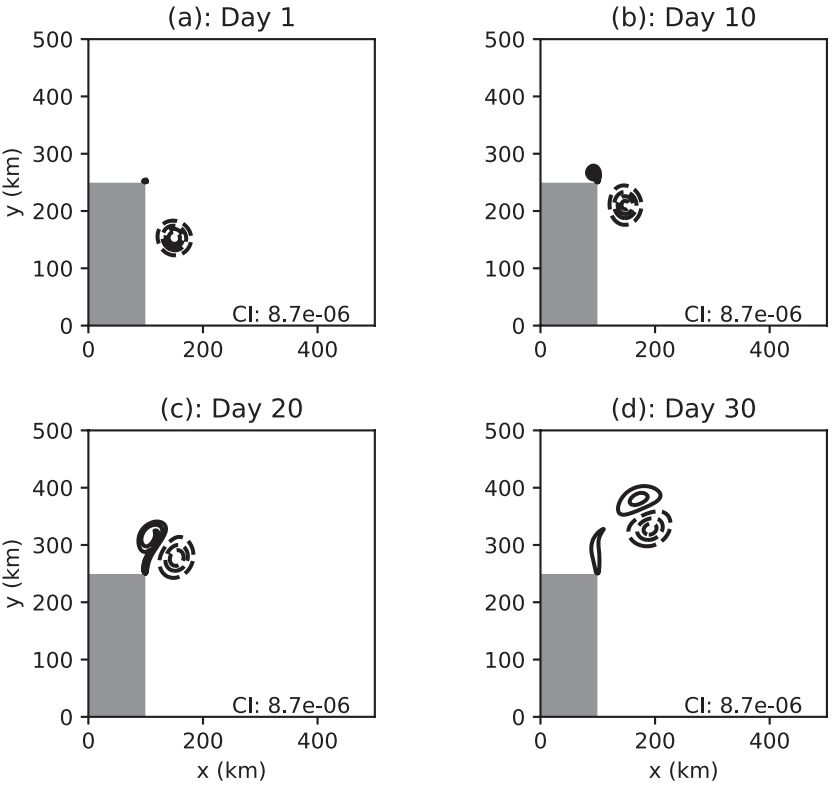

Figure 3. Time evolution of the vorticity field at (a) 1, (b) 10, (c) 20, and (d) 30 days. Dashed contours are negative values, and solid contours are positive values. Contour interval is 8.7×10^{-6} s^{-1}. The x- and y-axes are in kilometers.

to be extremely robust, self-propagating structures (Stern 1975; Nof 1990). A vorticity filament remains attached to the corner as a remnant of the previous interaction.

In the remainder of this article, we analyze the sequence of events just described to understand its consequences for the oceanic circulation. The main focus is to understand how positive vorticity has been generated at the corner. Is it the result of viscous processes, or is it generated via another mechanism? Can we quantify the amount of vorticity generated at the corner, and why does it form a dipole with the preexisting vortex? To what extent is this situation reminiscent of a realistic vortex-topography interaction in the ocean?

3. Vorticity creation

The sequence of events depicted in Figure 3 contain all of the ingredients that we wish to analyze (vortex propagation and vorticity creation). However, because little analytical

progress can be made with this model, we proceed to an additional level of simplification and replace the initial Gaussian vortex patch (equation 8) with a point vortex

$$\omega(r) = \frac{\Gamma_1}{2\pi}\delta(r), \tag{9}$$

which corresponds to the limit of the Gaussian patch (equation 8) as $r_0 \to 0$. The Gaussian patch can, in fact, be thought of as the result of viscosity on the point vortex (Saffman 1992).

a. Point vortex dynamics

The stream function ψ is related to the vorticity via Poisson's equation

$$\Delta\psi = -\omega. \tag{10}$$

Inverting this equation yields the stream function that is, in turn, used to get the velocity field to advect the vorticity. In an unbounded domain, when ω is given by equation (9), the solution of this equation is simply

$$\psi = -\frac{\Gamma_1}{2\pi}\log(r), \tag{11}$$

which is the Green's function of the Laplace operator in polar coordinates. If the vortex is placed next to a straight wall (semi-infinite domain), the latter imposes a no-normal-flow boundary condition. An easy way to solve equation (10) and satisfy the boundary condition is to use the method of images, which treats the wall as an axis of antisymmetry. In this framework, we solve Poisson's equation in an unbounded domain with two singularities of opposite sign (straddling the axis of antisymmetry). This pair of real plus imaginary vortices moves along this axis, as each vortex is advected by the flow created by its neighbor. The migration speed of the vortex near the wall is then

$$v_m = \frac{\Gamma_1}{4\pi d}, \tag{12}$$

where d is the distance between the vortex and the wall (Kundu and Cohen 2008). This analytical value of the migration speed for a point vortex compares well with the numerical value of the migration speed of a Gaussian bump (Fig. 3) as long as $d < 2r_0$ (not shown).

The next step is to take into consideration the presence of the corner (cf. Fig. 3). In such geometry, the boundary conditions are slightly more tedious to enforce. To circumvent this problem, the usual procedure to enforce no normal flow at the wall is to transform (via conformal mapping) the physical domain into a computational domain where the boundary conditions are easier to enforce. Such conformal mapping transforms a point vortex of strength Γ in the physical space into a point vortex of equal strength in the mapped space. In the remainder of this analysis, we denote by (x, y) the physical domain and (ξ, η) the computational domain. Moreover, we treat this problem in the complex plane, where

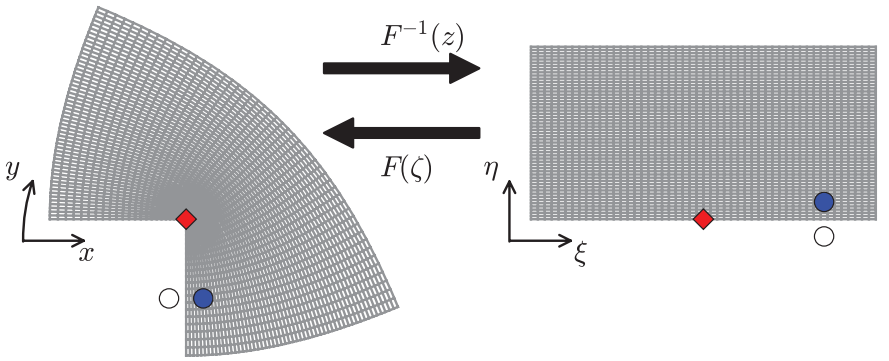

Figure 4. Illustration of the conformal mapping to switch from the physical domain (left) to the computational domain (right). The red diamond marks the position of the corner in the physical and mapped space. The blue dot marks the initial position of the (real) vortex, and the white dot marks the position of the corresponding image vortex.

$z = x+iy$ and $\zeta = \xi+i\eta$ are the complex coordinates. We consider the Schwartz-Christoffel mapping

$$z = F(\zeta) = e^{i\beta}\zeta^{\alpha/\pi}, \tag{13}$$

which maps the half plane $\mathrm{Im}(\zeta) > 0$ onto the wedge $\beta < arg(z) < \alpha + \beta$, and we call F^{-1} the reversed map. Figure 4 is the illustration of the transformation for $\alpha = 3\pi/2$, and $\beta = -\pi/2$, which corresponds to the transformation of the upper half plane onto the corner plotted in Figure 3. Note that the transformation is conformal everywhere except at the corner itself (red diamond in Fig. 4), where the transformation is singular [$F'(\zeta) = 0$]. The corner is located at $(0, 0)$ both in the physical and computational domain.

In the physical domain, we place a point vortex at $z = z_1$ next to the wall (blue point in Fig. 4), which is analogous to the configuration in Figure 3(a). The boundary condition at the wall is enforced in the mapped plane with the method of images such that the full complex potential in the mapped plane is

$$\psi(\zeta) = -\frac{i\Gamma_1}{2\pi}\log(\zeta - \zeta_1) + \frac{i\Gamma_1}{2\pi}\log(\zeta - \overline{\zeta_1}). \tag{14}$$

The equation of evolution of these vortices must be derived in the physical plane. We briefly recall the main steps of the derivation following the usual analytical development (see, e.g., Ferlauto 1997; Michelin and Llewellyn Smith 2009). By definition, the (complex conjugate) velocity field in the physical domain is given by

$$\overline{v}(z) = \frac{d}{dz}\psi[F^{-1}(z)] = \frac{1}{F'(\zeta)}\frac{d\psi(\zeta)}{d\zeta} = \frac{1}{F'(\zeta)}\overline{v}(\zeta), \tag{15}$$

where the overbar denotes the complex conjugate. In the problem we are considering, each point vortex is advected by the velocity field of the other vortices. We write ψ_j the corresponding stream function, which is the contribution of all vortices except the jth. Because the stream function is invariant under the conformal map transformation, the full stream functions in the physical and mapped planes are related by

$$\psi(z) = \psi_j(z) - \frac{i\Gamma_j}{2\pi}\log(z - z_j) = \psi_j(\zeta) - \frac{i\Gamma_j}{2\pi}\log(\zeta - \zeta_j) = \psi(\zeta). \tag{16}$$

In the physical plane, the velocity at z_j is given by

$$\frac{d\bar{z}_j}{dt} = \lim_{z\to z_i}\left\{\frac{d}{dz}[\psi_j(z)]\right\} = \lim_{z\to z_i}\left\{\frac{d}{dz}\left[\psi_j(\zeta) - \frac{i\Gamma_j}{2\pi}\log\left(\frac{\zeta - \zeta_j}{z - z_j}\right)\right]\right\}. \tag{17}$$

Using the chain rule for the z derivative and with a Taylor expansion around ζ_j (Clements 1973), we get the velocity field of the jth point vortex

$$\frac{d\bar{z}_j}{dt} = \frac{1}{F'(\zeta_j)}\left[\frac{d}{d\zeta}\psi_j(\zeta) + \frac{i\Gamma_j}{4\pi}\frac{F''(\zeta_j)}{F'(\zeta_j)}\right]. \tag{18}$$

The equation of motion of the point vortex j in the mapped plane is

$$\frac{d\bar{\zeta}_j}{dt} = \frac{1}{|F'(\zeta_j)|^2}\left[\frac{d}{d\zeta}\psi_j(\zeta) + \frac{i\Gamma_j}{4\pi}\frac{F''(\zeta_j)}{F'(\zeta_j)}\right]. \tag{19}$$

Because the conformal map is singular at $z = \zeta = 0$, $F'(0) = 0$, the flow is singular at the corner (see equation 15). In the limit of weak viscosity, the flow separates at that point and a discontinuity appears in the velocity field that can be described with a vortex sheet. This vortex sheet tends to roll up to itself to form a macrovortex (as seen in Fig. 3). As a first approximation, we treat this spiraled fluid as a point vortex of amplitude Γ_2 (Cortelezzi 1995). The magnitude of this secondary vortex is adjusted to remove the singularity in the total flow field at the corner with the usual procedure known as the Kutta condition. The full potential is given by the sum of the primary vortex, the secondary vortex, and their images

$$\psi(\zeta) = \sum_{j=1}^{2}\left[-\frac{i\Gamma_j}{2\pi}\log(\zeta - \zeta_j) + \frac{i\Gamma_j}{2\pi}\log(\zeta - \overline{\zeta_j})\right], \tag{20}$$

with Γ_1 the magnitude of the primary vortex and Γ_2 the magnitude of the secondary vortex. As long as the position ζ_2 of the secondary is known, we can use the Kutta condition $[\psi'(0) = 0]$ to get the value of Γ_2. In this framework, this condition is

$$\sum_{j=1}^{2}\Gamma_j\left(\frac{1}{\overline{\zeta}_j} - \frac{1}{\zeta_j}\right) = 0. \tag{21}$$

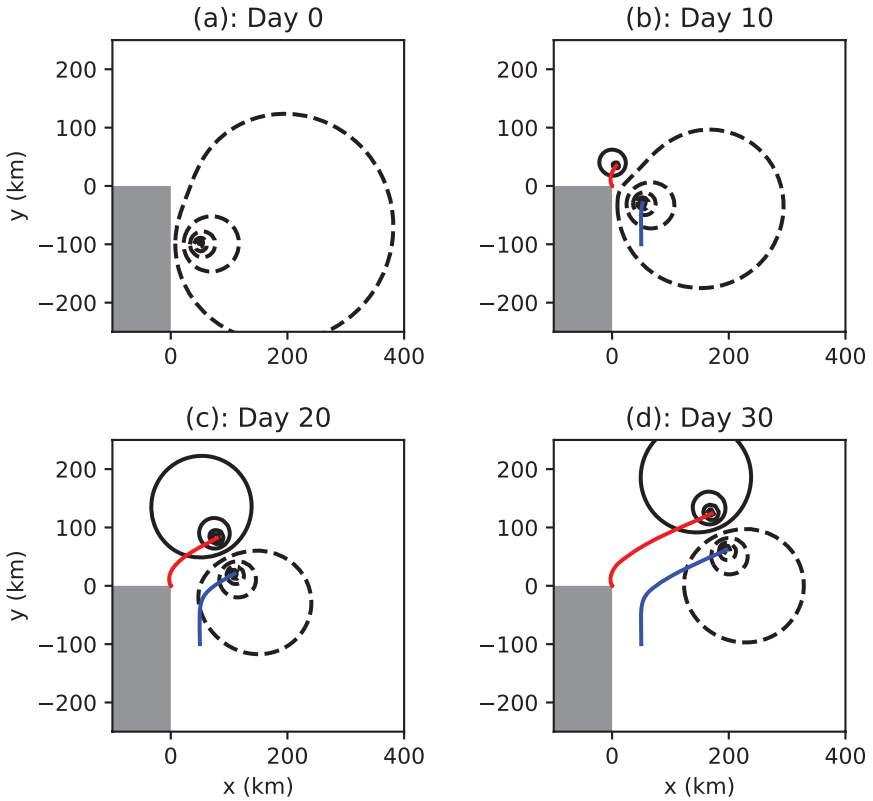

Figure 5. The blue and red lines mark the trajectory of the primary and secondary vortices, respectively. Time evolution of the stream function at (a) 0, (b) 10, (c) 20, and (d) 30 days. Dashed contours are negative values, and solid contours are positive values. Contour interval is 5.5×10^3 m^2 s^{-1}. The x- and y-axis are in kilometers.

We now proceed to the numerical integration of the system of equations (19) plus the Kutta condition (equation 21). We choose the parameters in order to match the original numerical simulation (Fig. 3). The system is integrated forward in time using an Adam-Bashforth third-order scheme. The results are plotted in Figure 5 where the contour lines are now the stream function (contrary to Fig. 3 where the contour lines were vorticity contours). The initial position of the anticyclone with respect to the wall is the same as in the preliminary experiment. As in the preliminary experiment, the vortex moves northward while its cyclonic companion grows at the corner (see also Fig. 6 for the time evolution of the magnitude of each vortex). As the primary vortex reaches the corner, it pairs up with the cyclone and the pair moves off the coast such that we get a fair agreement between the preliminary experiment and the present model.

In Figure 6, we compare the vorticity creation in the preliminary experiment and in the point vortex model. For the preliminary experiment, the solid red line is the integral of

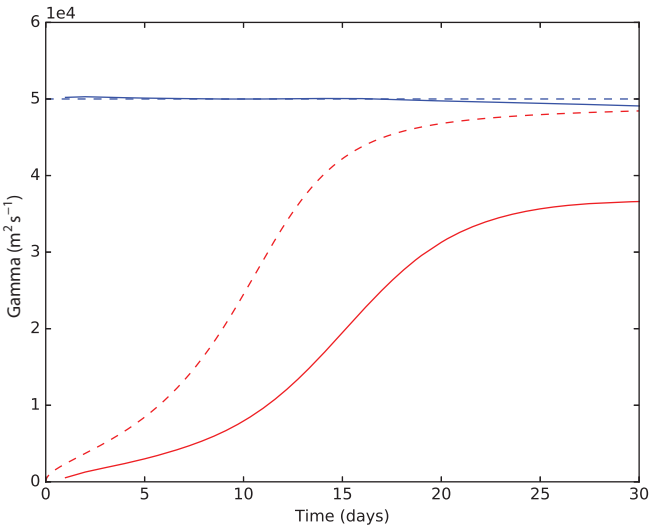

Figure 6. Comparison of the absolute value of vorticity contained in the primary vortex (blue line) and in the secondary vortex (red line) in the MIT general circulation model simulation (solid line) and in the point vortex model (dashed line).

positive vorticity and the solid blue line is minus the integral of negative vorticity in the domain. For the point vortex model, we plot with a dashed line the circulation $-\Gamma_1$ and Γ_2 in the primary and secondary vortex, respectively.

The amount of vorticity in the primary vortex appears to be very stable over the 30-day integration period (in the preliminary experiment, its amplitude may decay because of the presence of viscosity, and in the point vortex method, the amplitude Γ_1 is fixed). The magnitude of the secondary vortex Γ_2 increases in both models but reaches different values at the end of the integration. In the point vortex model, it asymptotically tends to $-\Gamma_1$ (dashed line), whereas the amount of positive vorticity created in the preliminary experiment is 25% lower in magnitude. This discrepancy is expected because the newly created point vortex is an average view of a rolled-up vortex sheet. In order to match the Kutta condition at the corner, the magnitude of the vortex is adjusted to create a nonsingular flow, whereas the vorticity creation really occurs on a vortex sheet at the tip of the corner. We conclude that the point vortex model is strongly constrained by geometric arguments such that the point vortex model overpredicts the vorticity creation. We also verify that the vorticity creation in the preliminary experiment does not depend on viscosity, even though a minimum amount of viscosity is required to stabilize the model (this aspect will be detailed further in Section 4b).

This discrepancy between the solid and dashed red curves in Figure 6 also has consequences for the subsequent evolution of the newly created dipole. In the point vortex model, the dipole is made up of two opposite signed vortices of almost equal strength such that the

pair is expected to travel along a straight line. By comparison, the dipole in the preliminary experiment is asymmetric, with the primary vortex 25% stronger than the newly created vortex. In such a configuration, the dipole follows a circular path (not shown). We conclude that the point vortex model gives a good qualitative overview of the system but fails to give a correct quantitative estimate of the vorticity creation. Regardless, it can still be regarded as an elegant way to view the evolution of the system.

b. Vortex sheet dynamics

To overcome the quantitative shortcomings of the previous section, we now use a pseudo–vortex sheet model for which the vortex sheet is approximated by a sum of blob vortices (Chorin 1973). This method is an alternative way to solve the Euler equations that is not routinely used in oceanography because of its poor convergence properties (Cottet and Koumoutsakos 2000). In fact, when we approximate a flow with a sum of point vortices without any particular precaution, it is easy to run into unphysical behavior when two vortices get close to each other (the velocity field of a point vortex is singular at its center). The method proposed by Chorin (1973) to overcome this issue is to smooth the velocity field generated by a point vortex near its center such that point vortices are now referred to as blob vortices. The stream function of each blob vortex is given by

$$\psi(r) = \begin{cases} \frac{-\Gamma}{2\pi}\log(r), & \text{if } r \geq \sigma \\ \frac{-\Gamma}{2\pi}\frac{r}{\sigma}, & \text{if } r < \sigma, \end{cases} \tag{22}$$

with σ a threshold chosen to guarantee numerical stability. The procedure to get the time evolution of each blob vortex is similar to the procedure described in the previous section, except that the sum (equation 20) is now computed over N vortices present in the flow. Note that the computation of the velocity at each blob vortex implies a double sum, which can be computationally demanding as the number of particles increases. To speed up the computation of this double sum, we use the fast multipole method algorithm (Greengard and Rokhlin 1987; Engblom 2011). The aim of this method is to group point vortices into clusters to reduce the number of interactions. A given vortex will feel the effect of several far-field clusters and neighbors. The far-field velocity of the clusters is computed efficiently with a Laurent series, and the influence of the neighbors is computed with a direct computation. Using this method, one can achieve an arbitrarily good level of accuracy by performing a multilevel evaluation of the velocity field (Greengard and Rokhlin 1987). To regularize the flow at the corner, we release a new vortex near the corner every M time steps, and we adjust the magnitude of each newly released vortex with the Kutta condition (which is a straightforward generalization of equation (21) with N vortices).

In Figure 7, we plot four snapshots of the integration of the blob vortex model in a configuration similar to that in Figure 3. The initial condition consists of an array of 10×10 point vortices. The magnitudes of these vortices are adjusted to reproduce the circulation of a Gaussian patch (equation 8). For visualization purposes, each blob vortex is represented

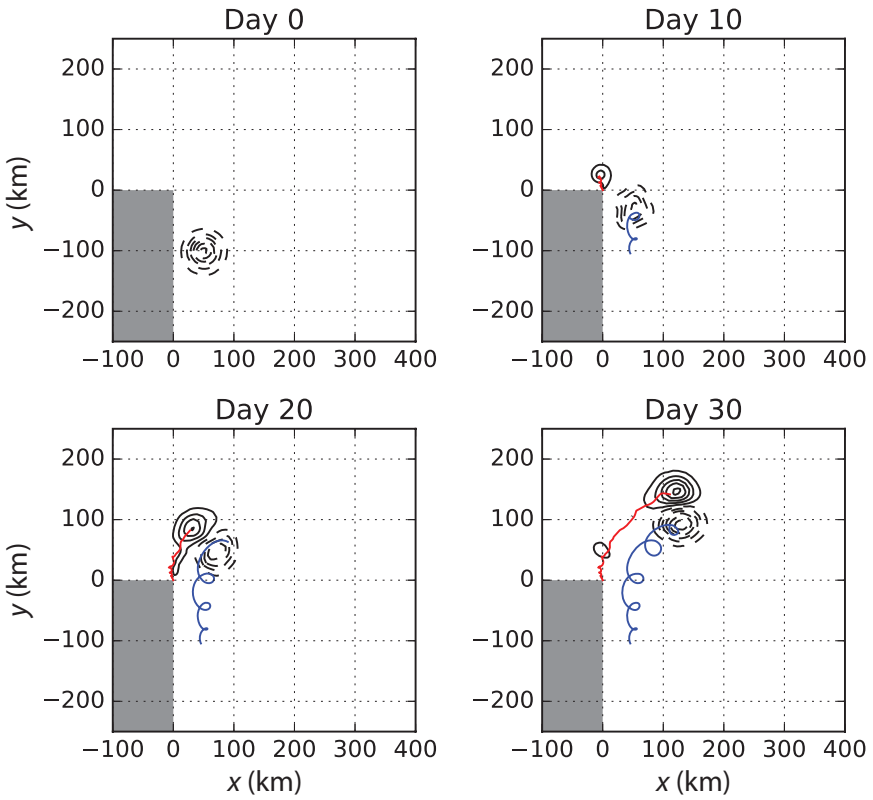

Figure 7. Vorticity evolution in the blob vortex model. The primary vortex is composed of an array of equally spaced vortices. The global vorticity field is reconstructed using a Gaussian kernel for each point vortex.

as a Gaussian distribution of width σ. The contour plot in Figure 7 is then the sum of all contributions of the blob vortices. We plot one trajectory of a blob vortex in the middle of the Gaussian patch in blue and the trajectory of the first vortex released at the corner in red. The four snapshots in Figure 7 are very similar to the preliminary experiment even though produced with two different models. Compared with the previous point vortex model, the distribution of vorticity is now more realistic (Gaussian patch). We verified that these results are insensitive to the precise choice of σ and M (not shown).

In Figure 8, we plot the vorticity budget for this blob vortex model and compare it with the preliminary experiment. Again, the amount of negative vorticity is stationary by definition, whereas the amount of positive vorticity increases as new vortices are constantly released. In this experiment, the number of degrees of freedom is greater than in the previous point vortex experiment where we had only one point vortex. In the present configuration, the (secondary) macrovortex grows in an asymmetric shape such that even if the Kutta condition is always satisfied, there is less vorticity injection in the system. It is no surprise that there

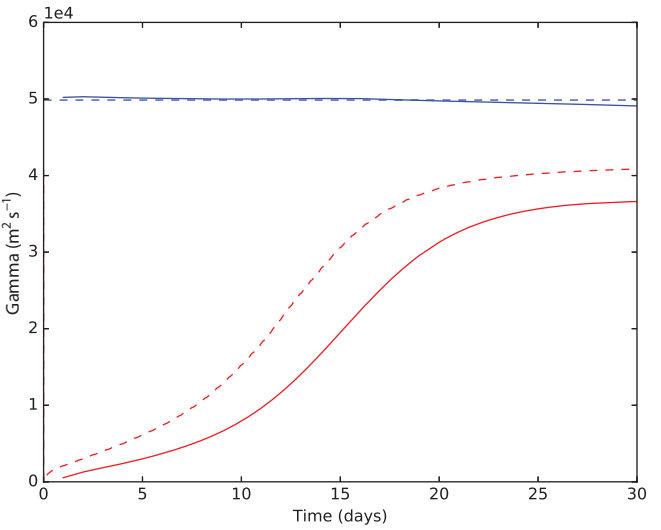

Figure 8. Same as Figure 6, but for the blob vortex model.

is not a perfect match between these two curves, because they come from a completely different discretization scheme. In fact, as we will describe in the next section, gridded models are not always suitable to handle discontinuity in the flow field.

4. Vorticity flux

We just showed that the preliminary experiment and the blob vortex are in fair agreement in terms of vorticity production and subsequent evolution of the vortices. However, the curves given in Figures 6 and 8 are only a numerical estimate of the vorticity creation for the configuration in Figures 3, 5, and 7. Our goal is now to derive an analytical formula for the vorticity flux for an arbitrary configuration.

a. Inviscid limit

The Navier-Stokes vorticity equation (equation 1) can be written as

$$\frac{\partial \omega}{\partial t} + \nabla . \boldsymbol{J} = 0, \tag{23}$$

with $\boldsymbol{J}$ the generalized vorticity flux. In the idealized framework with no external forcing and no dissipation, $\boldsymbol{J}$ simply corresponds to the advection of vorticity

$$\boldsymbol{J} = \boldsymbol{u}\omega. \tag{24}$$

This term is zero at the boundary because of the no-normal-flow boundary condition, except at the corner where there is a discontinuity in the flow field (Cottet and Koumoutsakos 2000). To see how this discontinuity matters, we write the Euler equation in velocity vorticity form

$$\frac{\partial \boldsymbol{u}}{\partial t} - \boldsymbol{u} \times \omega = -\nabla P - \frac{1}{2}\nabla(|\boldsymbol{u}|^2). \tag{25}$$

We integrate this equation over a contour $\mathcal{C}$ corresponding to the coastline to obtain an expression of the circulation around this contour

$$\frac{\partial}{\partial t}\int_{\mathcal{C}} \boldsymbol{u} \cdot \boldsymbol{t} dl = \frac{1}{2}\left(|\boldsymbol{u}(C^+)|^2 - |\boldsymbol{u}(C^-)|^2\right), \tag{26}$$

where we used the identity $(\boldsymbol{u} \times \omega) \cdot \boldsymbol{t} = \omega \boldsymbol{u} \cdot \boldsymbol{n} = 0$ on $\mathcal{C}$. We also implicitly used the Kutta condition that guarantees the continuity of the pressure field at the singularity. The velocities $\boldsymbol{u}(C^+)$ and $\boldsymbol{u}(C^-)$ are taken on each side of the singularity. Using the Stokes theorem, we equate the circulation in equation (26) with the integral of vorticity in the domain

$$\frac{\partial}{\partial t}\int_S \omega = \frac{1}{2}\left[\boldsymbol{u}(C^+) + \boldsymbol{u}(C^-)\right]\left[\boldsymbol{u}(C^+) - \boldsymbol{u}(C^-)\right]. \tag{27}$$

This equation demonstrates how the discontinuity in the flow field is related to a vorticity injection into the system. We only get an integral rate for the vorticity injection into the system, which can be directly related to equation (23). In fact, we can interpret $1/2[\boldsymbol{u}(C^+) + \boldsymbol{u}(C^-)]$ as the advection velocity and $\boldsymbol{u}(C^+) - \boldsymbol{u}(C^-)$ the strength of the vortex sheet that is injected into the system. Note that even if the vorticity injection appears as a completely inviscid mechanism, we used the implicit assumption of viscosity to regularize the flow (Kutta condition)—this is why we call it a pseudoinviscid mechanism. For the corner problem, we have $\boldsymbol{u}(C^-) = 0$, such that the time rate of change of the vorticity is given by

$$\frac{\partial}{\partial t}\int_S \omega = \frac{1}{2}U^2, \tag{28}$$

with U the velocity at the corner. Interestingly, Spall (2014) derived a similar scaling for a domain without discontinuities but with no-slip boundary conditions.

b. Vorticity creation in numerical models

We just derived the vorticity flux in the inviscid limit and showed that this vorticity flux is independent of viscosity. The next logical question is whether this vorticity flux is accurately captured in gridded models. We already know that the vorticity production in the blob vortex model and in the preliminary experiment matches relatively well, but we want to understand the effect of the discretization in gridded models. Indeed, the theoretical vortex sheet that enters the domain at the corner involves a discontinuity in the velocity field that gridded models usually struggle to capture. In principle, there are four elements that might be relevant in this problem: the discretization of the viscous operator, the value of the viscosity, the discretization of the advection scheme, and the horizontal grid resolution.

In an attempt to better understand the effect of the viscous operator on piecewise-constant topography, Adcroft and Marshall (1998) showed that the discretization of this operator has

a strong effect on the solution. We briefly recall their result here and see how it can be adapted to our corner problem. The viscous operator can be written as

$$\begin{aligned} \nu\nabla^2 u &= \partial_x F^{ux} + \partial_y F^{uy} \\ \nu\nabla^2 v &= \partial_x F^{vx} + \partial_y F^{vy}, \end{aligned} \tag{29}$$

with

$$\boldsymbol{F} = \begin{bmatrix} F^{ux} & F^{uy} \\ F^{vx} & F^{vy} \end{bmatrix} \tag{30}$$

the viscous stress tensor. From a numerical modeling point of view, the three main ways to write this tensor are

$$\boldsymbol{F}_c = \begin{bmatrix} \nu\partial_x u & \nu\partial_y u \\ \nu\partial_x v & \nu\partial_y v \end{bmatrix} \tag{31}$$

$$\boldsymbol{F}_s = \begin{bmatrix} \nu(\partial_x u - \partial_y v) & \nu(\partial_y u + \partial_x u) \\ \nu(\partial_x v + \partial_y u) & \nu(\partial_y v - \partial_x u) \end{bmatrix} \tag{32}$$

$$\boldsymbol{F}_{vd} = \begin{bmatrix} \nu(\partial_x u + \partial_y v) & \nu(\partial_y u - \partial_x u) \\ \nu(\partial_x v - \partial_y u) & \nu(\partial_y v + \partial_x u) \end{bmatrix}, \tag{33}$$

which are the conventional form, the symmetric form, and the vorticity-divergence form, respectively. Shchepetkin and O'Brien (1996) and Adcroft and Marshall (1998) showed that the choice of a given formulation strongly affects the solution. Shchepetkin and O'Brien (1996) were interested in the interaction between a dipole and a seamount. In their case, the symmetric tensor was producing the least amount of spurious vorticity. Adcroft and Marshall (1998) were interested in modeling the large-scale gyre circulation as a function of the steppiness of the topographic coastline. In the problem they were considering, they saw the vorticity injection as a spurious numerical effect attributable to the discretization of the coastline; whereas in our case, the position of the boundary is exactly known, and the vorticity injection is a desired effect.

The second numerical choice is the discretization of the advection operator. For standard finite volume ocean models, the two main choices are the flux form, where the momentum flux is computed at each side of a cell, and the vector invariant form (equation 25). The vector invariant advection scheme has been developed to conserve energy and vorticity (Arakawa 1966; Sadourny 1975). We shall see that this is true only if it is used in conjunction with the vorticity-divergence viscous operator (equation 33).

i. Vorticity budget for the flux form advection and conventional viscosity operator The test case shown in Figure 3 was computed with the flux form momentum equation and the conventional viscous operator. To evaluate the validity of equation (28) in this context, we compute at each time step the total amount of vorticity present in the system. A time

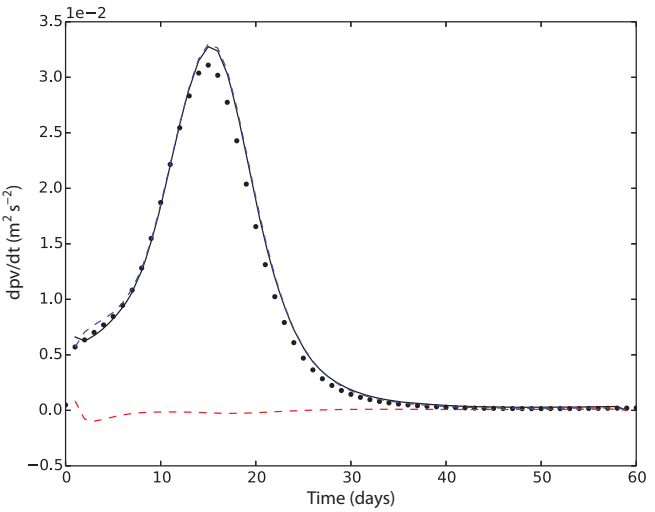

Figure 9. Vorticity budget for the two-dimensional simulation shown in Figure 3 (numerical and analytical). The dotted line corresponds to equation (28) (inviscid limit), whereas the solid black line is the time derivative of the integrated vorticity content in the model. The two components of this time derivative are the advective component (dashed blue line, almost indistinguishable from the solid black line) and the viscous flux (dashed red line).

differentiation of this time series gives an estimate of the left-hand side of equation (28) and is plotted with a solid black curve in Figure 9. This curve corresponds to the time derivative of the solid red curve in Figure 8. In the same figure, we plot with a dotted line the right-hand side of equation (28), with U evaluated one-half grid point away from the corner (v_1 in Fig. 10). We also plot with a dashed blue line the vorticity flux attributable to the advective operator and with the dashed red line the vorticity flux attributable to the viscous operator (so that the sum of the dashed blue and dashed red line corresponds to the solid black curve). The first interesting element is the good agreement between the vorticity budget and the pseudoinviscid vorticity budget given in equation (28). We then notice that the total vorticity flux is almost entirely attributable to the advective term. Both elements confirm that an inviscid mechanism is at the source of the vorticity creation at the corner.

In Figure 10, we plot the position of the velocity and vorticity points in a staggered C-grid. The velocities u_0 and v_0 fall on the boundary and are then equal to zero. On this grid, the vorticity is defined at the corner of each grid cell and is zero at the boundary with the free-slip boundary condition. In fact, when we perform the vorticity budget, we do the integral on all interior vorticity points not considering the vorticity points on the coastline. There is, however, an ambiguity for the corner point (ζ_0 in Fig. 10) that is not part of the vorticity budget per se. According to the vorticity budget, the only way to explain the advective flux of vorticity in the domain is if $\zeta_0 \neq 0$, which is in contradiction with the definition of the

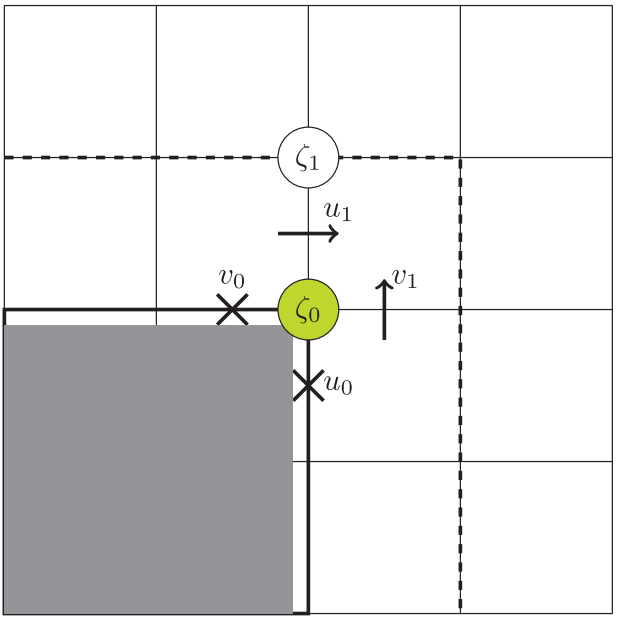

Figure 10. Staggered grid near the corner.

free-slip boundary condition: if $\zeta_0 = (v_1 - u_1)/\Delta x$, then we recover a nonzero advection of vorticity inside the domain. The ambiguity comes from the fact that the vortex sheet that emanates from the corner is supposed to be infinitely thin, which is impossible to capture with such a gridded model.

We repeat the same experiment for different values of the viscosity coefficient. For lower values of ν, subgrid-scale noise appears near the corner and contaminates the solution. We find, however, that the integral vorticity budget still holds for these noisy solutions (not shown). This subgrid-scale noise disappears if we increase the grid resolution (not shown). For higher values of the viscosity coefficient, the vortex spreads more rapidly (as expected) and the vorticity budget changes. In Figure 11, we plot the vorticity budget and the vorticity map at day 30 for a similar configuration but with $\nu = 100\ \mathrm{m^2\ s^{-1}}$. We first notice in the vorticity budget that equation (28) is now slightly different from the numerical vorticity budget (it is also different from the vorticity budget shown in Figure 9 because the velocity at the corner is weaker in the present case). Again, the main contribution of the vorticity flux comes from the advective component, but now the frictional component is larger. This tendency increases as the viscosity coefficient increases (not shown).

ii. Vorticity budget with the vector invariant form and for the symmetric viscous tensor
We now switch the advection scheme to the vector invariant form and use the symmetric tensor for the viscous operator. The results are shown in Figure 12 for $\nu = 20\ \mathrm{m^2\ s^{-1}}$ and in

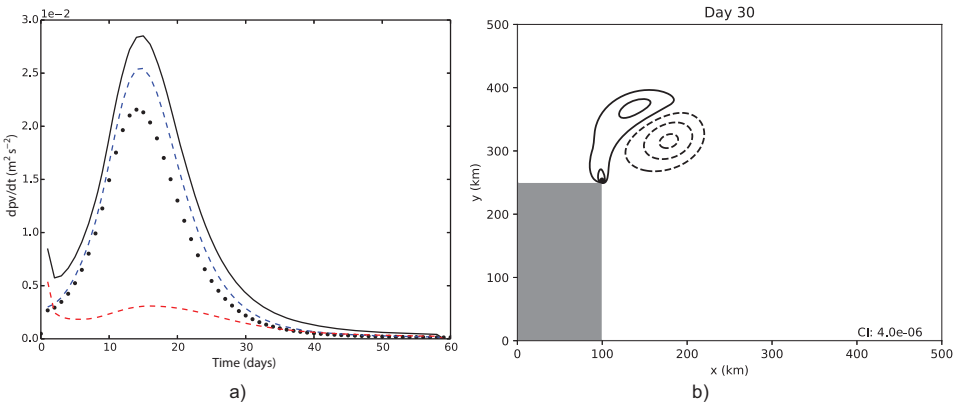

Figure 11. (a) Vorticity budget for the experiment conducted with the flux form and conventional viscosity operator and $\nu = 100\ \mathrm{m^2\,s^{-1}}$. (b) Snapshot of the vorticity for this experiment at day 30.

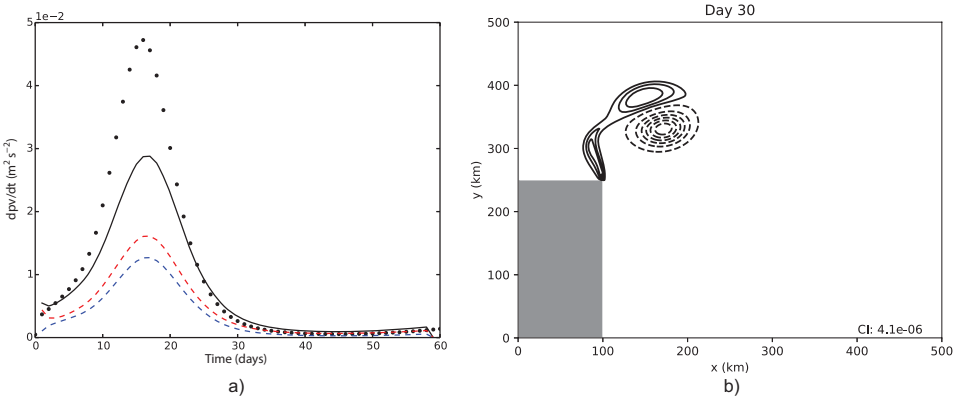

Figure 12. Vector invariant form and symmetric viscous tensor with $\nu = 20\,\mathrm{m^2\,s^{-1}}$. (a) Vorticity budget. (b) snapshot of the vorticity at day 30.

Figure 13 for $\nu = 100\,\mathrm{m^2\,s^{-1}}$. The vorticity patterns at day 30 look similar to Figure 3(d) and Figure 11(b) respectively. However, in the first case ($\nu = 20\,\mathrm{m^2\,s^{-1}}$), equation (28) overpredicts the vorticity generation, whereas in the second case, it underpredicts it. There is, in fact, good agreement between equation (28) and the effective vorticity production for $\nu = 50\,\mathrm{m^2\,s^{-1}}$ (not shown). What is interesting in this case is to decompose again the total vorticity flux into the advective and viscous component. In both cases, the viscous operator is the main contributor to the vorticity injection. As the viscosity increases, this term becomes more and more important.

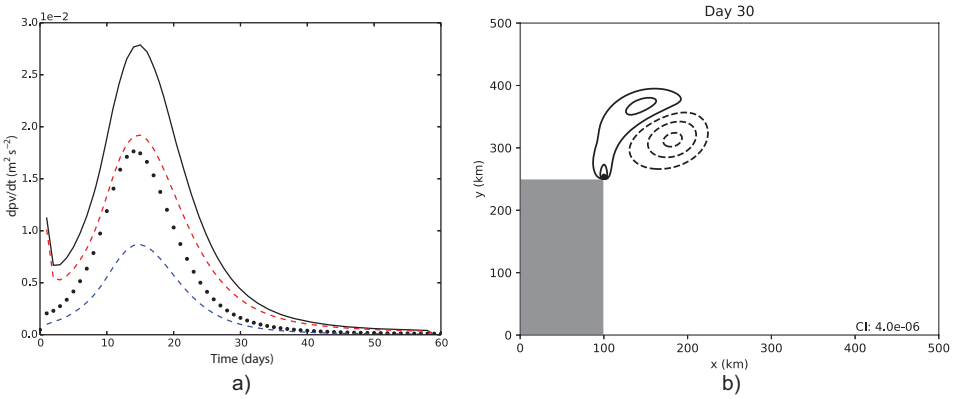

Figure 13. Same as Figure 12, but with $\nu = 100\ \mathrm{m^2\ s^{-1}}$.

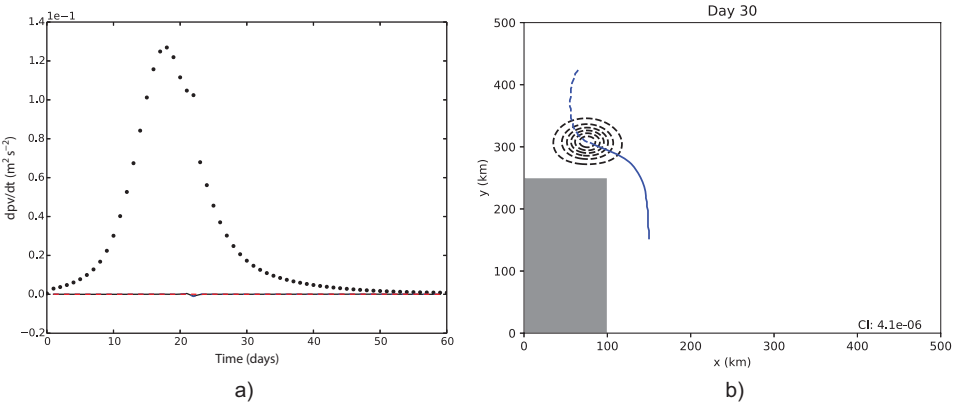

Figure 14. Simulation with the vector invariant form and the viscosity-divergence viscous operator, with $\nu = 20\ \mathrm{m^2\ s^{-1}}$. (a) vorticity budget. (b) Snapshot of the vorticity at day 30. The trajectory prior to day 30 is plotted with a solid blue line and the trajectory between day 30 and day 60 is plotted with a dashed blue line.

iii. Vorticity budget with the vector invariant for and the vorticity-divergence viscous tensor

In this configuration, we keep the vector invariant form for the advection scheme and choose the vorticity-divergence viscous operator with $\nu = 20\ \mathrm{m^2\ s^{-1}}$. The results shown in Figure 14 are radically different from all previous experiments. In this case, there is almost no vorticity creation, and the vortex turns around the corner (the trajectory is plotted with a blue line in Fig. 14b). After turning the corner (day 30), the vortex collides with the wall located at $x = 0$ and continues its northward migration (dashed blue line). The fact that the vortex turns around the corner is actually what we expect from a purely inviscid model with free-slip

boundary conditions. As a consequence, we obtain a nonrealistic behavior of the vortex near the corner. Lastly, we notice that for the chosen grid size, a value of $\nu > 5\ \mathrm{m^2\ s^{-1}}$ was necessary to guarantee the stability of the model. Higher values of ν only affect the spread of the primary vortex but do not change the global behavior (still no vorticity creation at the corner).

In this section, we were able to derive an analytical formula for the vorticity flux at the corner and test it in various numerical formulations. Equation (28) provides an accurate description of the vorticity flux in the barotropic case with the flux form advection scheme. We showed that the vector invariant scheme is less suited to represent the vortex sheet discontinuity because this scheme is meant to conserve vorticity. The next step is to add degrees of realism to this simple model to see how active this vorticity production is in more realistic configurations.

5. Discussion: Toward more realistic solutions

The previous solutions were in a nonrotating system, although the addition of a constant Coriolis parameter does not affect the vorticity equation. However, we anticipate that the β effect will affect the vorticity budget.

a. The β effect

The β effect is a consequence of the latitudinal gradient of the Coriolis parameter. Llewellyn Smith (1997) showed that it is possible to solve the vorticity equation on a β plane for a single point vortex using asymptotic expansions. He was able to recover the usual westward drift of cyclones and anticyclones under the effect of β. Another possibility to capture this effect is to model a macroscopic vortex with a cloud of point vortices (as in Section 3b) and use the following conservation equation:

$$\frac{D}{Dt}(\omega + \beta y) = 0. \tag{34}$$

The conserved quantity is no longer the relative vorticity, but instead is the absolute vorticity. For the initial condition, we assign a strength Γ_j to each point vortex. In the subsequent evolution, if the jth vortex moves northward or southward, its strength is adjusted to keep its absolute vorticity equal to the initial value. Using this technique, Velasco Fuentes and Velázquez Muñoz (2003) showed that, with a minimal model composed of two point vortices to represent a macrovortex, one could get a westward β drift of correct magnitude. In fact, a pair of two identical vortices rotates at an angular velocity of $\Gamma/\pi h$, where h is the distance between the two vortices. On the β plane, the strength of these vortices will vary as they rotate such that, on average, the pair of vortices self-propagate westward. This minimal model is a crude representation of the β effect but still captures the main features of the dynamics.

There are, however, two drawbacks to this method. First, the entire domain must be seeded with point vortices, even regions where the initial condition has zero relative vorticity. This is required because the background flow will advect (initially passive) vortices north and south. Such advection will trigger a vorticity change in these vortices (far-field effect). This aspect is not a limitation, per se, but if we must carry the integration for a large number of vortices, we may lose the efficiency of the vortex methods. The second limitation lies in the numerical implementation of this method. The strength Γ of a point vortex is usually interpreted as its circulation with units of $\mathrm{m}^2\,\mathrm{s}^{-1}$ while βy has units of s^{-1}. To reconcile these two units, one needs to arbitrarily assign an area for the point vortex at which vorticity will be affected by the β effect.

As mentioned earlier, the two main effects attributable to β are (1) the westward drift for both cyclones and anticyclones and (2) the intensity decrease (amplification) as an anticyclone moves northward (southward)—the opposite is true for a cyclone. Hence, in the case of the NBC rings, as well as for the idealized corner problem, the anticyclone will lose intensity as it approaches the barrier of an island (the corner). At this latitude, $f_0 = 2.5 \times 10^{-5}\ \mathrm{s}^{-1}$ and $\beta = 2.2 \times 10^{-11}\ \mathrm{m}^{-1}\,\mathrm{s}^{-1}$. For a vortex of size $R \sim 100$ km, the westward drift is about $v_w = \beta R^2 = 0.2\ \mathrm{m\,s}^{-1}$, which is of the same order of magnitude as the observed NBC ring translation speed (see Section 1). The theoretical eddy migration speed along a wall (given in equation 12) depends on the ring magnitude and its distance to the wall. As the ring approaches the corner, the vorticity production also depends on the ring magnitude and its distance to the wall. There are two possible scenarios at the corner: the first is the dipole formation that we have described earlier; the second involves the β effect such that the rings start drifting westward north of the corner even if vorticity is still created at the corner. To characterize the onset of one or the other scenario, we form a nondimensional number

$$\alpha = \frac{\Gamma}{4\pi R^3 \beta}, \tag{35}$$

which corresponds to the ratio of the migration speed of the eddy along the wall and its westward drift. We postulate that for $\alpha \gg 1$, the β effect should be unimportant, and we should recover the scenario illustrated in Figure 3. For $\alpha \ll 1$, the westward drift should be the dominant effect and with no dipole formation.

Being aware of the aforementioned limitation of the point vortex model, we proceed to the numerical integration of equation (34). In this article, we do not consider far-field effects so that we do not place initially inert vortices in the background flow. In Figure 15, we illustrate the dynamics for $\alpha = 0.5$. There is still vorticity generation at the corner, but once the primary vortex is north of the corner, then the β drift overcomes the dipole propagation. The scenario for $\alpha > 1$ is very similar to Figure 7 (not shown). For the case of the NBC rings, we estimated $\Gamma = 8 \times 10^5\ \mathrm{m}^2\,\mathrm{s}^{-1}$ in the HYCOM reanalysis (Chassignet et al. 2009) such that $\alpha \simeq 3$, which would be in favor of the dipole formation scenario.

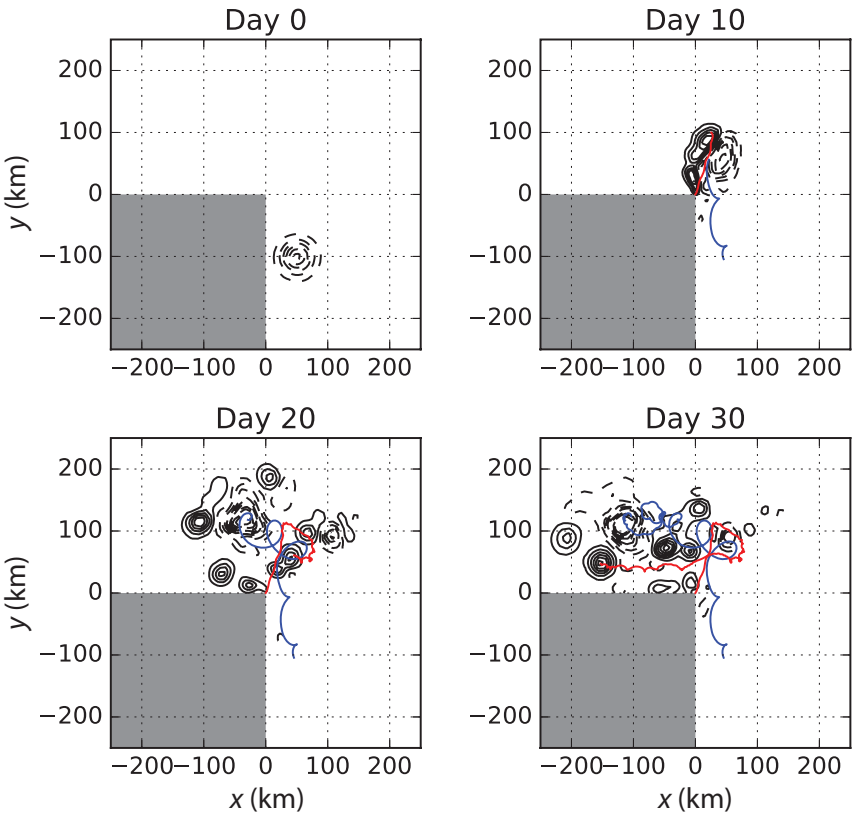

Figure 15. Same as Figure 7, but on the β plane. In this configuration, $\alpha = 0.5$.

6. Conclusions

In this article, we focused on the migration of oceanic eddies along the coast and their separation from the coast. Using a simple point vortex formalism, we were able to retain the main characteristics of this migration. We highlighted a pseudoinviscid mechanism that is responsible for vorticity creation at singular points on the coast. This vorticity generation is a robust feature across several models, and we were able to validate the inviscid vorticity budget (equation 28) to measure the associated vorticity injection.

The main limitation of this mechanism is that it must involve a singularity at the boundary. Of course, such singularities almost never exist in nature. In practice, we need to appeal to the no-slip boundary condition such that a thin vortex sheet of viscous origin is present at the boundary. This boundary layer detaches near sharp topographic features in the same way as in the inviscid corner problem. For example, the classic case of flow past a cylinder was introduced in the oceanographic community by Marshall and Tansley (2001). Tansley and Marshall (2001) computed a threshold to diagnose the boundary layer separation in the

presence of β effect. In order to do a numerical simulation of the boundary layer detachment, we would need a very high-resolution model with immersed boundary conditions (Tseng and Ferziger 2003) to handle the realistic viscous vortex sheet with the no-slip boundary condition. A problem related to piecewise constant boundary lines has already been emphasized by Adcroft and Marshall (1998). They demonstrated that such a representation adds an artificial friction in the model (which is consistent with the mechanism described in this article). However, their large-scale solutions at the gyre scale looked qualitatively the same regardless of the discretization scheme. In the problem that we are interested in addressing, the choice of the discretization will have a strong impact on the dynamics of the eddy.

Some additional interesting points remain to be understood if we are to connect this article to the realistic NBC rings dynamics. A natural extension would be to consider a more realistic two-layer model (White and McDonald 2004; Nilawar, Johnson, and McDonald 2012; Southwick, Johnson, and McDonald 2016). In a two-layer model, the stream function of a point vortex is a linear combination of the log profile and K_0 Bessel function. Contrary to the barotropic system, which has no characteristic length scale, the baroclinic system is strongly influenced by the presence of the deformation radius. This deformation radius will directly impact the migration speed of a vortex against the wall and the vorticity production.

Also in this article, we barely touched on the trajectory of the dipole, and we did not mention at all its interactions with the chain of islands. The first impression when looking at ocean simulations of this region is that the chain of islands serves as a propagation guide for the dipole (Fratantoni and Richardson 2006). Many studies have considered the break up of oceanic eddies against a chain of islands (Simmons and Nof 2002; Cenedese, Adduce, and Fratantoni 2005), but the propagation of an eddy along the islands remains to be understood.

Another important parameter that we did not consider in this study is the role of the background flow and the interactions between eddies. Also, once an eddy leaves the coast or propagates along the chain of islands, it may leak (Shi and Nof 1994) and affect the dynamics of subsequent eddies. To account for this effect, we would need to consider a model where eddies are shed periodically and consider their mutual interaction.

Furthermore, in our investigation of inviscid vorticity production, it should be noted that one such inviscid mechanism is the Kelvin wave arrest described in Dewar and Hogg (2010) and Dewar, Berloff, and Hogg (2011). We have not attempted to connect the Kelvin wave problem and the present approach (i.e., Kelvin wave near singularities), but this topic will be addressed in a future study.

Last but not least, we stress again that according to the mechanism developed in this article, there is no enstrophy conservation near singular topographic features: as soon as a flow interacts with a corner, the system will start shedding vorticity filaments in the system. This is a crucial element with regard to the energy and enstrophy cascades in the ocean. In classic quasi-geostrophic dynamics, the inverse cascade is responsible for transferring energy from small scales to larger scales. The process that we highlighted here is responsible for creating fine-scale filaments and may lead to new regimes of turbulence.

Acknowledgments. The authors thank D. Marshall, an anonymous referee, and G. Roullet for helpful comments that improved the manuscript greatly. Funding for this research was provided by National Science Foundation (award 1434780).

REFERENCES

Adcroft, A., and D. Marshall. 1998. How slippery are piecewise-constant coastlines in numerical ocean models? Tellus Ser. A, *50*, 95–108. doi: 10.1034/j.1600-0870.1998.00007.x.

Arakawa, A. 1966. Computational design for long-term numerical integrations of the equations of atmospheric motion: Two-dimensional incompressible flow. Part I. J. Comput. Phys., *1*, 119–143. doi: 10.1016/0021-9991(66)90015-5.

Brøns, M., M. C. Thompson, T. Leweke, and K. Hourigan. 2014. Vorticity generation and conservation for two-dimensional interfaces and boundaries. J. Fluid Mech., *758*, 63–93. doi: 10.1017/jfm.2014.520.

Cenedese, C., C. Adduce, and D. M. Fratantoni. 2005. Laboratory experiments on mesoscale vortices interacting with two islands. J. Geophys. Res.: Oceans, *110*, C09023. doi: 10.1029/2004JC002734.

Chassignet, E. P., and Z. D. Garraffo. 2001. Viscosity parameterization and the gulf stream separation, *in* From Stirring to Mixing in a Stratified Ocean, P. Müller and D. Henderson, eds. Honolulu: School of Ocean and Earth Science and Technology, University of Hawaii, 37–41.

Chassignet, E. P., H. E. Hurlburt, E. J. Metzger, O. M. Smedstad, J. A. Cummings, G. R. Halliwell, R. Bleck, et al. 2009. US GODAE: global ocean prediction with the hybrid coordinate ocean model (HYCOM). Oceanography, *22*, 64–75.

Chassignet, E. P., and D. P. Marshall. 2008. Gulf stream separation in numerical ocean models, *in* Ocean Modeling in an Eddying Regime, M. Hecht and H. Hasumi, eds. Geophysical Monograph 177. Washington, DC: American Geophysical Union, 39–61.

Chorin, A. J. 1973. Numerical study of slightly viscous flow. J. Fluid Mech., *57*, 785–796. doi: 10.1017/S0022112073002016.

Clements, R. R. 1973. An inviscid model of two-dimensional vortex shedding. J. Fluid Mech., *57*, 321–336. doi: 10.1017/S0022112073001187.

Cortelezzi, L. 1995. On the unsteady separated flow past a semi-infinite plate: Exact solution of the Brown and Michael model, scaling, and universality. Phys. Fluids, *7*, 526–529. doi: 10.1063/1.868765.

Cottet, G.-H., and P. D. Koumoutsakos. 2000. Vortex Methods: Theory and Practice. Cambridge: Cambridge University Press.

Deremble, B., A. M. Hogg, P. Berloff, and W. K. Dewar. 2011. On the application of no-slip lateral boundary conditions to 'coarsely' resolved ocean models. Ocean Modell., *39*(3–4), 411–415. doi: 10.1016/j.ocemod.2011.05.002.

Dewar, W. K., P. Berloff, and A. M. Hogg. 2011. Submesoscale generation by boundaries. J. Mar. Res., *69*, 501–522. doi: 10.1357/002224011799849345.

Dewar, W. K., and A. M. Hogg. 2010. Topographic inviscid dissipation of balanced flow. Ocean Modell., *32*, 1–13. doi: 10.1016/j.ocemod.2009.03.007.

Engblom, S. 2011. On well-separated sets and fast multipole methods. Appl. Numer. Math., *61*, 1096–1102. doi: 10.1016/j.apnum.2011.06.011.

Ferlauto, M. 1997. Studio e controllo di strutture vorticose di parete. PhD diss. Milan, Italy: Polytechnic University of Milan.

Fratantoni, D. M., and D. A. Glickson. 2002. North Brazil Current ring generation and evolution observed with SeaWiFS. J. Phys. Oceanogr., *32*, 1058–1074. doi: 10.1175/1520-0485(2002)032%3C1058:NBCRGA%3E2.0.CO;2.

Fratantoni, D. M., and P. L. Richardson. 2006. The evolution and demise of North Brazil Current rings. J. Phys. Oceanogr., *36*, 1241–1264. doi: 10.1175/JPO2907.1.

Garraffo, Z. D., W. E. Johns, E. P Chassignet, and G. J. Goni. 2003. North Brazil Current rings and transport of southern waters in a high resolution numerical simulation of the North Atlantic. Elsevier Oceanography Series, *68*, 375–409. doi: 10.1016/S0422-9894(03)80155-1.

Greengard, L., and V. Rokhlin. 1987. A fast algorithm for particle simulations. J. Comput. Phys., *73*, 325–348. doi: 10.1016/0021-9991(87)90140-9.

Johns, W. E., R. J. Zantopp, and G. J. Goni. 2003. Cross-gyre transport by North Brazil Current rings. Elsevier Oceanography Series, *68*, 411–441. doi: 10.1016/S0422-9894(03)80156-3.

Kundu, P. K., and I. M. Cohen. 2008. Fluid Mechanics, 4th ed. Amsterdam: Academic Press.

Llewellyn Smith, S. G. 1997. The motion of a non-isolated vortex on the beta-plane. J. Fluid Mech., *346*, 149–179. doi: 10.1017/S0022112097006290.

Lundgren, T., and P. Koumoutsakos. 1999. On the generation of vorticity at a free surface. J. Fluid Mech., *382*, 351–366. doi: 10.1017/S0022112098003978.

Marshall, D. P., and C. E. Tansley. 2001. An implicit formula for boundary current separation. J. Phys. Oceanogr., *31*, 1633–1638. doi: 10.1175/1520-0485(2001)031%3C1633:AIFFBC%3E2.0.CO;2.

Marshall, J., A. Adcroft, C. Hill, L. Perelman, and C. Heisey. 1997. A finite-volume, incompressible Navier Stokes model for studies of the ocean on parallel computers. J. Geophys. Res.: Oceans, *102*, 5753–5766. doi: 10.1029/96JC02775.

Michelin, S., and S. G. Llewellyn Smith. 2009. An unsteady point vortex method for coupled fluid-solid problems. Theor. Comput. Fluid Dyn., *23*, 127–153. doi: 10.1007/s00162-009-0096-7.

Morton, B. R. 1984. The generation and decay of vorticity. Geophys. Astrophys. Fluid Dyn., *28*, 277–308. doi: 10.1080/03091928408230368.

Nilawar, R. S., E. R. Johnson, and N. R. McDonald. 2012. Finite Rossby radius effects on vortex motion near a gap. Phys. Fluids, *24*(6), 066601. doi: 10.1063/1.4721432.

Nof, D. 1990. Modons and monopoles on a γ-plane. Geophys. Astrophys. Fluid Dyn., *52*, 71–87. doi: 10.1080/03091929008219840.

Sadourny, R. 1975. The dynamics of finite-difference models of the shallow-water equations. J. Atmos. Sci., *32*(4), 680–689. doi: 10.1175/1520-0469(1975)032%3C0680:TDOFDM%3E2.0.CO;2.

Saffman, P. G. 1992. Vortex Dynamics. New York: Cambridge University Press.

Shchepetkin, A. F., and J. J. O'Brien. 1996. A physically consistent formulation of lateral friction in shallow-water equation ocean models. Mon. Weather Rev., *124*, 1285–1300. doi: 10.1175/1520-0493(1996)124%3C1285:APCFOL%3E2.0.CO;2.

Shi, C., and D. Nof. 1994. The destruction of lenses and generation of wodons. J. Phys. Oceanogr., *24*, 1120–1136. doi: 10.1175/1520-0485(1994)024%3C1120:TDOLAG%3E2.0.CO;2.

Simmons, H. L., and D. Nof. 2002. The squeezing of eddies through gaps. J. Phys. Oceanogr., *32*, 314–335. doi: 10.1175/1520-0485(2002)032%3C0314:TSOETG%3E2.0.CO;2.

Southwick, O. R., E. R. Johnson, and N. R. McDonald. 2016. A simple model for sheddies: Ocean eddies formed from shed vorticity. J. Phys. Oceanogr., *46*, 2961–2979. doi: 10.1175/JPO-D-15-0251.1.

Spall, M. A. 2014. Some influences of remote topography on western boundary currents. J. Mar. Res, *72*(2), 73–94. doi: 10.1357/002224014813758968.

Stern, M. E. 1975. Minimal properties of planetary eddies. J. Mar. Res, *33*(1), 1–13.

Tansley, C. E., and D. P. Marshall. 2001. Flow past a cylinder on a β plane, with application to Gulf Stream separation and the Antarctic Circumpolar Current. J. Phys. Oceanogr., *31*, 3274–3283. doi: 10.1175/1520-0485(2001)031%3C3274:FPACOA%3E2.0.CO;2.

Tseng, Y.-H., and J. H. Ferziger. 2003. A ghost-cell immersed boundary method for flow in complex geometry. J. Comput. Phys., *192*, 593–623. doi: 10.1016/j.jcp.2003.07.024.

Velasco Fuentes, O. U., and F. A. Velázquez Muñoz. 2003. Interaction of two equal vortices on a β plane. Phys. Fluids, *15*, 1021–1032. doi: 10.1063/1.1556293.

Verron, J., and E. Blayo. 1996. The no-slip condition and separation of western boundary currents. J. Phys. Oceanogr., *26*, 1938–1951. doi: 10.1175/1520-0485(1996)026%3C1938:TNSCAS%3E2.0.CO;2.

White, A. J., and N. R. McDonald. 2004. The motion of a point vortex near large-amplitude topography in a two-layer fluid. J. Phys. Oceanogr., *34*, 2808–2824. doi: 10.1175/JPO2658.1.

Zhai, X., H. L. Johnson, and D. P. Marshall. 2010. Significant sink of ocean-eddy energy near western boundaries. Nat. Geosci., *3*, 608–612. doi: 10.1038/ngeo943.

Received: *25 July 2016*; revised: *7 December 2016*.